American Mineralogist, Volume 81, pages 1321–1331, 1996

An XAFS study of the crystal chemistry of Fe in orthopyroxene

C. Closmann,[1] E. Knittle,[1] and F. Bridges[2]

[1]Earth Science Department and Institute of Tectonics, University of California, Santa Cruz, California 95064, U.S.A.
[2]Physics Department and Institute of Tectonics, University of California, Santa Cruz, California 95064, U.S.A.

Abstract

X-ray absorption fine-structure (XAFS) spectra at the Fe *K* edge in Bamble enstatite $(Mg_{0.88}Fe_{0.12})SiO_3$ were analyzed in conjunction with theoretical XAFS spectra to determine the bonding configuration of Fe in this structure. The structural analysis involved determination of the Fe distribution between the octahedral M1 and M2 sites, and Fe-O bond lengths in the M2 site, into which Fe strongly partitions. Our analysis yielded bond lengths for Fe in the M2 site of 1.97(2), 1.98(2), 2.09(2), 2.16(2), 2.43(2), and 2.65(10) Å, in agreement with bond lengths determined from X-ray and neutron-diffraction analysis of the two orthopyroxene end-members. The average Fe-O bond length in the M2 site is 2.22(2) Å, longer than that of the Mg end-member (2.151 Å) but approximately the same as that of the Fe end-member (2.228 Å) of the orthopyroxene solid-solution series. Octahedral distortion of the M2 site may be greater than that of either the Fe or Mg end-member. The presence of a minor amount of Fe^{3+} was inferred by our analysis of the M1 site and was also suggested by our bond-valence calculations, which yielded a charge of 2.07 for Fe in the M2 site and a charge of 2.78 for Fe in the M1 site. Simple calculations using our data and those of other studies show that the average Fe-O bond length in the M2 site is constant along the Fe-Mg join in the orthopyroxene solid-solution series.

Introduction

The site distribution and bonding configuration of Fe in enstatitic orthopyroxene have been extensively studied using various experimental techniques, including XAFS (Mottana et al. 1990; Farges et al. 1994), X-ray diffraction (Pollack and Rubie 1964; Domeneghetti and Steffen 1992; Skogby et al. 1992; Sykes-Nord and Molin 1993), Mössbauer spectroscopy (Bancroft et al. 1967; Evans et al. 1967; Virgo and Hafner 1968; Domeneghetti and Steffen 1992; Skogby et al. 1992), and optical absorption spectroscopy (Bancroft and Burns 1967; Goldman and Rossman 1976). The crystal-chemical behavior of Fe in orthopyroxene is largely controlled by the distribution of Fe between two sites: a relatively undistorted octahedral site (M1) and a highly distorted octahedral site (M2). Much experimental work has shown that Fe preferentially fills the distorted M2 octahedron in orthopyroxene, and that disorder of Fe between the M1 and M2 sites increases with increasing equilibration temperature. Thus, the Fe site distribution is useful in determining equilibration temperatures of orthopyroxene-bearing rocks (Ghose 1965; Ghose and Hafner 1967; Virgo and Hafner 1970; Smyth 1973; Ukhanov and Malysheva 1973; Ganguly and Ghose 1979; Gupta and Mendiratta 1980; Molin 1989; Sykes-Nord and Molin 1993). The Fe content of orthopyroxene has been demonstrated to play an important role in upper mantle geochemistry (e.g., Stolper 1980; Longhi 1991; Kinzler and Grove 1992a, 1992b), and Fe site partitioning between orthopyroxene and other phases is likely controlled by the temperature dependence of Fe ordering between the M1 and M2 sites (von Seckendorff and O'Neill 1993). Therefore, accurate crystal-chemical characterization of Fe in orthopyroxene is crucial for a thorough understanding of mantle geochemistry.

In spite of the vast literature on orthopyroxene, no detailed XAFS study has been published on the site distortion around Fe in the orthopyroxene structure. Farges et al. (1994) conducted an XAFS study of enstatite similar to ours, yet their analysis did not include detailed models for bond lengths and site partitioning. Their study did, however, show that XAFS modeling of orthopyroxene is particularly useful in modeling other high-pressure polymorphs, such as $(Mg,Fe)SiO_3$ perovskite. In addition, Mottana et al. (1990) obtained XAFS data on orthopyroxene from granulites, showing that XAFS determination of M1 and M2 site distribution was compatible with Mössbauer experiments on the same orthopyroxene.

The potential for extensive use of XAFS in characterizing mineral structures depends on a thorough understanding of the strengths and limitations of the technique for studying the typically disordered and distorted structures of many minerals (cf. Waychunas et al. 1986; Mottana et al. 1990; Farges et al. 1994). Therefore, we investigated the structure of enstatite, a mineral well characterized by other techniques, to test the accuracy and sensitivity of XAFS analysis in determining site distortion and bond lengths for the Fe crystallographic sites. Using experimental data in conjunction with theoretical XAFS

0003–004X/96/1112–1321$05.00

TABLE 1. Composition of Bamble enstatite starting material from microprobe analysis

Constituent	Wt%
MgO	34.22(0.69)
TiO	0.03(0.05)
MnO	0.05(0.03)
NiO	0.05(0.15)
SiO_2	56.19(0.59)
FeO	8.54(0.14)
CaO	0.29(0.04)
Al_2O_3	0.05(0.03)
Total	99.38

standards, we determined the site distortion in the M2 site in enstatite, roughly verified previous results of Fe site partitioning in enstatite, and demonstrated the high quality of the theoretical XAFS functions generated by the computer code FEFF5, recently developed by Rehr and coworkers (Rehr and Albers 1990; Rehr et al. 1991; Mustre de Leon et al. 1991). We could not compare our results directly with those of Farges et al. (1994) because their model was simpler, using one-O and two-O shells. Consequently, their results include contributions from atoms on both the M1 and M2 sites in enstatite, whereas we modeled the two sites separately. Finally, although our errors for site distribution of Fe are large, a precedent has been set for use of XAFS in both site-distortion and site-distribution determination, and we anticipate that theoretical modeling of XAFS spectra can be a powerful tool for analysis of the crystal-chemical behavior of other cations in distorted crystallographic sites.

EXPERIMENTAL METHODS

A sample of natural enstatite $[(Mg_{0.88}Fe_{0.12})SiO_3]$ from Bamble, Norway, was used in this XAFS study. The composition was determined by microprobe analyses and is given in Table 1. Although our microprobe results do not account for Fe^{3+} in the sample, previous studies of Bamble enstatite indicate that Fe^{3+} accounts for <5% of the Fe in the sample (Bancroft and Burns 1967; Bancroft et al. 1967; Goldman and Rossman 1976, 1977; Rossman 1980).

The enstatite was powdered to ~5 μm size under acetone and brushed evenly onto pieces of Scotch tape. Each sample consisted of two double layers of tape, corresponding to about one absorption length. The samples were examined under an optical microscope (magnification of 400×) to ensure that the samples were uniform and that no pinholes were present. Transmission XAFS measurements on the Fe *K* edge (7110 eV) were collected at a temperature of 84 K using beamline 10-2 of the Stanford Synchrotron Radiation Laboratory (SSRL). An Si(111) monochromator was used, and the Si crystals were detuned 40–50% from maximum intensity to minimize harmonics of the desired photon energy. The slit size in front of the sample was 0.7 (vertical) by 1.8 mm (horizontal). Such narrow slits were used to minimize monochromator-induced glitches in the XAFS data

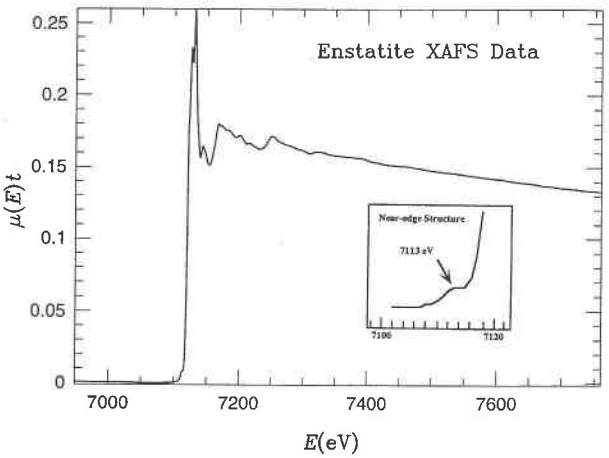

FIGURE 1. XAFS spectrum for enstatite sample. The preedge background was subtracted. The absorption edge is at ~7119 eV, and we used the XAFS oscillations out to ~7700 eV. The inset shows closeup of near-edge feature at 7113 eV, which indicates the presence of a distorted site and which has been attributed to a 1s → 3d state transition (Waychunas et al. 1983; Farges 1995).

(Bridges et al. 1992). Energy resolution using this experimental configuration was ~1.2 eV at the Fe *K* edge. Measurements were made using gas-ionization counters containing N_2 gas, and a third counter simultaneously measured the intensity passing through a reference sample to monitor shifts in the energy of the monochromator.

DATA ANALYSIS AND RESULTS

Data reduction

A standard series of procedures (Hayes and Boyce 1982; Teo 1986; Li et al. 1995) was used to reduce the data. The slowly decreasing preedge background absorption was subtracted to observe absorption resulting from only the atom of interest (Bridges et al. 1995). Figure 1 shows the raw spectrum of the enstatite data (an average of three scans) in electron volts after removal of the preedge background. A preedge peak, due to a 1s → 3d state transition (Waychunas et al. 1983; Farges 1995), appears in the enstatite spectrum and indicates significant distortion of the primary site into which Fe^{2+} partitions in the structure. XAFS oscillations extended to ~7700 eV, or 12.5 $Å^{-1}$ in reciprocal space (*k* space) above the absorption edge. The limited *k* range and the damping of our XAFS signal result from disorder of Fe in the enstatite structure.

A spline function was fitted to the data above the absorption edge to determine the atomic absorption, μ_0, and the starting point of the XAFS fit was optimized as described in Li et al. (1995). Once μ_0 has been determined, the XAFS function $\chi(E)$ is determined as follows:

$$\chi(E) = [\mu(E) - \mu_0(E)]/\mu_0(E) \quad (1)$$

where $\mu(E)$ includes the XAFS oscillations. Because the more useful XAFS formulation, $k\chi(k)$, is a function of the

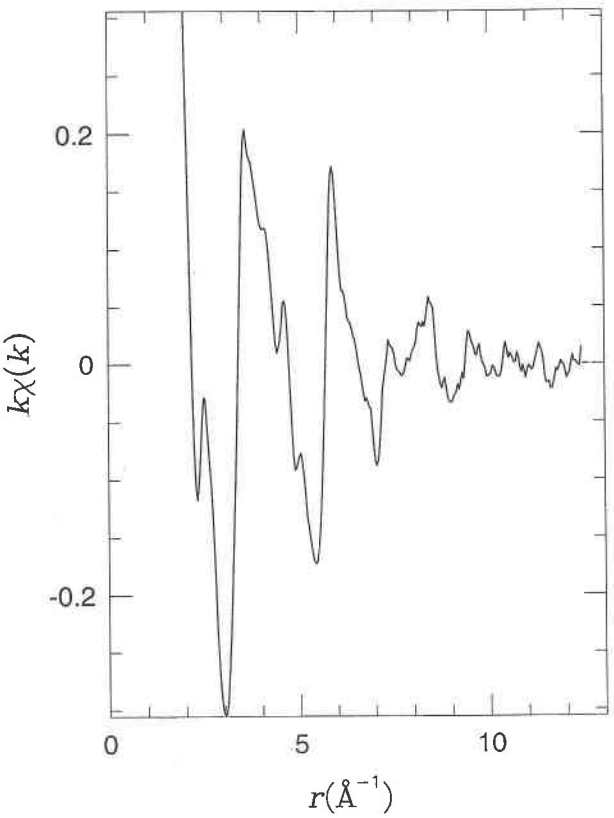

FIGURE 2. XAFS data of the k space at the Fe K edge in $(Mg,Fe)SiO_3$ enstatite.

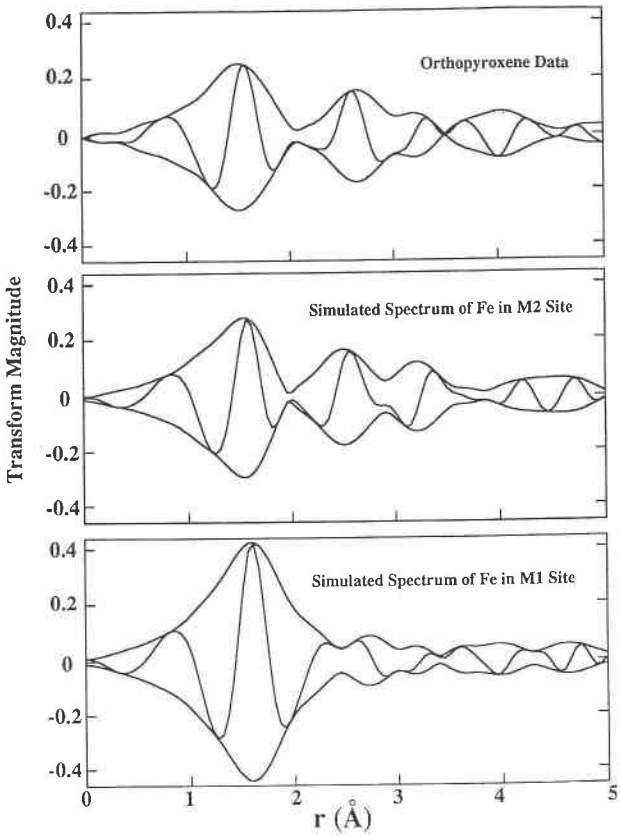

FIGURE 3. Fourier transforms of the XAFS data and synthetic XAFS spectra for Fe in the M1 and M2 sites. The outer envelope is the magnitude of the FT $[\pm(Re^2 + Im^2)^{1/2}]$, and the inner curve represents the real part of the transform. Note that the zero crossings of the inner curve closely match those of the data and M2 synthetic spectra out to 2.2 Å. The bond distances plotted here were uncorrected for phase shift and so are ~0.5 Å shorter than the actual bond lengths.

photoelectron wave vector **k**, the data must be converted from photon energy, E, to k (in inverse angstroms) using the equation

$$k = [2m(E - E_0)]^{1/2}/\hbar \quad (2)$$

where m is the mass of an electron, $\hbar$ is $h/2\pi$, where h is Planck's constant, E is the incident photon energy in electron volts, and E_0 is the energy at the absorption edge. The resulting XAFS equation in terms of the wave vector, $k\chi(k)$, is given by

$$k\chi(k) = \Sigma\, [N_j F_j(k)/r_j^2]\sin[2kr_j + \phi_j(k)] \times \exp(-2k^2\sigma_j^2 - 2r_j/\lambda) \quad (3)$$

where the sum is over all atomic shells with N_j atoms at a distance r_j from the absorbing atom, k is given by Equation 2, $F_j(k)$ is the backscattering amplitude, $\phi_j(k)$ is the phase shift of the photoelectron resulting from its interaction with the backscattering and absorbing atoms, σ_j is the Debye-Waller factor for r_j, and λ is the effective electron mean free path. Figure 2 shows the k-space XAFS data for our enstatite sample. The k-space data were Fourier transformed to yield spectra in real space with peaks corresponding to the radial distances, R, of neighboring atoms from the central absorbing atom: We used a Fourier transform (FT) range of 2.0–12.5 Å^{-1}, Gaussian rounded by 0.3 Å^{-1}. The FT of $k\chi(k)$ must be compared to standard compounds or theoretical calculations to determine the phase shifts at the scattering and absorbing atoms. In Figure 3 we show an XAFS spectrum in r space (real space, in angstroms), along with the two theoretically calculated XAFS spectra, for Fe in the M2 and M1 sites, generated as described in the next section. Note that r-space distances in Figure 3 are offset from the actual bond distances by phase shifts induced by the scattering neighbor atoms and by the absorbing atom. The r-space phase shift varies for different scattering atoms and is typically ~0.4 Å for O in the first-neighbor shell around Fe atoms.

Generation of theoretical XAFS standards

The ab initio X-ray absorption fine-structure code FEFF5 version 5.03 of Rehr and coworkers (Rehr and Albers 1990; Rehr et al. 1991; Mustre de Leon et al. 1991), which includes curved-wave effects, was used to generate the theoretical XAFS standards (i.e., simulated XAFS spectra). For absorbing atoms with atomic num-

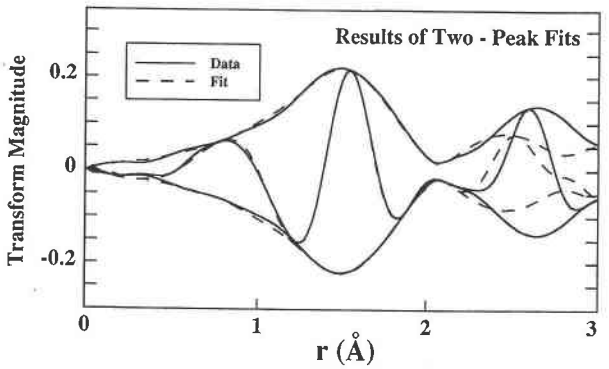

FIGURE 4. Fourier transform of the XAFS data (solid lines) and the best fit using a sum of two synthetic XAFS spectra for Fe in the M2 site (dashed lines). The fit used to generate this plot included the range between 1.2 and 2.5 Å, excluding phase-shift effects.

bers similar to that of Fe, these calculated spectra are in excellent agreement with experimental standards: Typically errors are 0.005 Å for nearest-neighbor distances and 5–6% for amplitude (Li et al. 1995). Using the lattice and positional parameters of enstatite determined by Ghose et al. (1986), we generated the local structure around Fe (out to 7 Å) in the M1 and M2 sites in enstatite. We then calculated the entire XAFS spectra [hereafter referred to as Fe(M1) and Fe(M2)] for Fe in both the M1 and M2 sites, using FEFF5. In addition, we generated standards for individual atom pairs: Fe-O, Fe-Si, and Fe-Fe, to model our spectra for individual bond distances. Finally, we generated a set of standards, which excluded the six nearest O neighbors surrounding the Fe in both the M1 and M2 sites but included the higher atomic shells: Hereafter, we refer to these models as M1outer and M2outer. These particular standards were used to complement models for the individual Fe-O bond distances of the six nearest neighbors.

As a first approximation, the theoretical XAFS spectrum generated assuming that Fe occupies only the M2 site in enstatite compares much more favorably to our XAFS data than does the theoretical spectrum for Fe on the M1 site (see Fig. 3). In Figure 3, we note that zero crossings of the real part of the FT (inner curve) for the data and the theoretical Fe(M2) XAFS spectra overlap almost completely in the first-neighbor shell and agree reasonably well out to 2.7 Å. In contrast, the Fe(M1) theoretical XAFS spectrum does not agree as well with the data for the first-neighbor shell and differs dramatically above 2.05 Å.

Fitting procedure

To verify that Fe substitutes predominantly into the M2 site and not the M1 site, to determine the individual Fe-O bond distances, and to constrain the degree of distortion of the M1 site, we ran nonlinear least-squares fits using the FIT2 routine of the Physics Department of the University of California, Santa Cruz. This routine models the r-space spectrum using a sum of standard functions for each peak in the Fourier transform: A set of peaks with bond distances that are too close to resolve are treated as one peak. The goodness-of-fit parameter, $(R\%)^2$ (Li et al. 1995), is minimized for different sets of initial conditions and assumptions. We first modeled the data to determine the general site distribution of Fe between the M1 and M2 sites in the orthopyroxene structure (preliminary model). More detailed fits, using results from the preliminary model and previous work, were designed to determine (1) individual Fe-O bond lengths (model A) and (2) distortion of the M1 site (model B).

Preliminary model

We first quantified the visual observations described above, that the data appear most similar to the theoretical XAFS spectra for Fe on the M2 site, by fitting the data as the sum of the two theoretical standards Fe(M1) and Fe(M2). These fits ignored the relative distortions of each site and required an overall magnitude, a global σ (broadening parameter), and a net relative position in r space for each site. The fits were performed in r space over the range 1.2–2.5 Å, which includes the dip in the spectrum at ~2.05 Å characteristic of Fe(M2). The best fits indicated that 79 ± 5% of the Fe is in the M2 site, with the remainder in the M1 site. The fits required a small total expansion (~0.02 Å) of the M2 site relative to the total expansion that would be expected from substituting Fe into the Mg end-member (Ghose et al. 1986) and a significant contraction for Fe in the M1 site. Input parameters were varied widely in terms of the fractional occupation of Fe on the M2 site but consistently converged to the same range of values under the constraint that the M1 and M2 site distortions remain unchanged. In Figure 4 we show the best fit to the data using this procedure. The fact that this simple sum of the two synthetic XAFS spectra so closely resembles the enstatite data up to 2.1–2.2 Å indicates the sites are only slightly distorted from the theoretical standards.

For the fits shown, seven parameters were allowed to vary: two bond distances, two amplitudes (which were constrained to sum to 100%), two σ values, and one E_0, which was equal for both standards. For our study, the theoretically allowed number of variables was calculated from Stern (1993) using

$$N = [(2\Delta k \Delta R)/\pi] + 2. \quad (4)$$

Here, Δk is (12.5 − 2.0) Å^{-1} and ΔR is (2.5 − 1.2) Å. Therefore, the total number of independent variables that we could expect to extract from our data is ~11. The number of fit parameters in the more detailed models, A and B, described below are approximately equal to this theoretical number of independent variables, and thus we attempt to extract the maximum amount of information from the XAFS spectra. Indeed, these models were designed to examine the limits of the XAFS technique. Yet, because there is independent information on the crystallography of enstatite (for example, bond lengths from

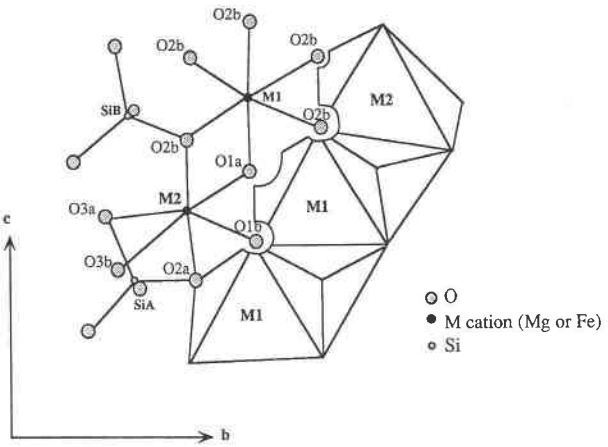

FIGURE 5. Model of M1 and M2 sites in the enstatite structure. Large shaded circles are O atoms, black circles are M2 cations, small shaded circles are Si atoms.

X-ray diffraction), such starting information, along with results from the preliminary model and theoretical XAFS spectra, can be used to fix some of the parameters in the XAFS analysis. Such fixing of parameters allowed us to extract a detailed picture of the bond distances and site distortions of Fe in enstatite.

Model A

Model A was designed to determine the six individual Fe-O bond distances for the M2 site. The M2 site in orthopyroxene is quite distorted, and the six Fe-O bonds exhibit slightly different crystal-chemical behavior. We use the standard crystallographic notation for the six O atoms to which Fe bonds in this site: O1a, O1b, O2a, O2b, O3a, and O3b atoms, as shown in Figure 5. The letter suffixes refer to the tetrahedral chain of which the O atom is a member. O3 atoms, the farthest from the M2 cations, form the bridging O atoms in tetrahedral chains and are thus overbonded and expected to form the weakest Fe-O bonds. In contrast, the two shortest Fe-O bonds involve the more strongly bound O1 atoms. Intermediate between these two extremes are the O2 atoms (Hawthorne and Ito 1977; Cameron and Papike 1980; Ghose 1982; Ghose et al. 1986). Thus, the strength or weakness of the Fe-O bond is manifested in its relative variability in length upon substitution of one cation for another and in its relative distance from Fe in the M2 site.

To model the XAFS spectra, we fitted for the six individual nearest-neighbor O-atom distances of Fe in the M2 site. In this fit, the higher atomic shells surrounding Fe in the M2 site were fixed using a composite sum of all other bond distances in the Fe(M2) spectrum (M2outer). To model Fe in the more ideal M1 site, we used the entire Fe(M1) spectrum. For initial estimates of the Fe-O bond distances in the M2 site, we used bond distances for both Mg–end-member and Fe–end-member orthopyroxene. A series of fits were run in which Fe site distribution between the M2 and M1 sites was cycled through possible values of M2 site occupancy starting at 100% and extending to 73%. To maintain a sufficiently large fit range to determine bond distances in the M2 site while minimizing the number of parameters varied, we found that the optimal fit range in r space was 1.2–2.5 Å. Results generated in this manner included fits with ten adjustable parameters (six bond distances for the six individual Fe-O bond distances in the M2 site, two σ values for M1outer and M2outer, one amplitude-reduction factor, and E_0) and 11 or 12 adjustable parameters (seven or eight Fe-O bond distances, two σ values for M1outer and M2outer, one amplitude-reduction factor, and E_0). In fitting for six Fe-O distances, the number of fit parameters (ten) is within the theoretical estimate for the maximum number of parameters that can be extracted from our data (~11; see above). When we included one or two additional bond distances in the fitting procedure, we did not improve the fit to the XAFS data over the ten-parameter models and appeared to have reached the limit of the amount of information that can be extracted from the XAFS data, in accord with the theoretical estimate of the number of fit parameters.

TABLE 2. Best fit results for M2 distances: Model A

Atom*	Distance (Å)		
	This study	Mg end-member**	Fe end-member†
O2b	1.97(2)	1.9921	1.994
O2a	1.98(2)	2.0333	2.024
O1b	2.09(3)	2.0567	2.129
O1a	2.16(2)	2.0891	2.158
O3a	2.43(2)	2.2881	2.460
O3b	2.65(10)	2.4474	2.600

* For O-atom positions, refer to Figure 5.
** Pure Mg–end-member (enstatite) bond distances from Ghose et al. (1986).
† Pure Fe–end-member (ferrosilite) bond distances from Sueno et al. (1976).

Acceptable fits to the XAFS data were achieved for all reasonable values of M2 site distribution [100% < Fe^{M2}/(Fe^{M2} + Fe^{M1}) < 76%] when σ for individual Fe-O peaks was fixed at 0.03. We note that our results are not overly sensitive to σ: Changing the σ values by 0.01 affected the bond distances by <0.01. Table 2 shows the results from the model-A fits for M2 site bond lengths. Our fits consistently converged to these bond lengths (± the error reported in Table 2) for the different starting estimates of Fe-O distances, different fit ranges, and different values of Fe site distribution. In Figure 6 we show the resulting model XAFS spectrum in comparison with the data.

Differences in amplitude of the M2 site between 100 and 76% M2 contribution resulted in the following changes for the Fe-O bond distances. The first two bond distances consistently converged to 1.97(2) and 1.98(2) Å for all M2 site distribution percentages. The third bond distance converged to 2.08(2)–2.10(2) Å, depending on Fe site distribution: In Table 2 we report this distance as an average value of 2.09(3) Å. The fourth bond distance

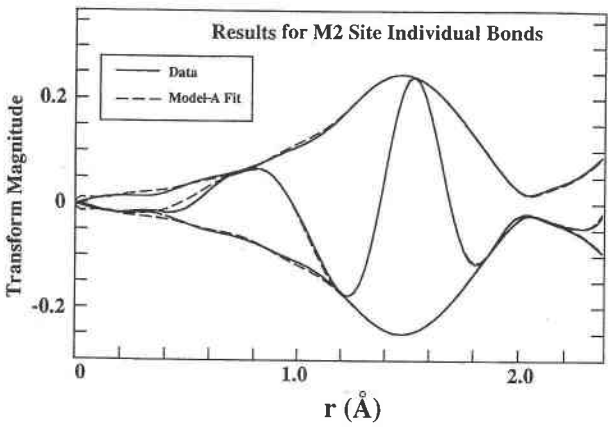

FIGURE 6. Fourier transform of the XAFS data (solid lines) and fit to the data (dashed lines) using model A. Fits extended to 2.4 Å without the phase shift and include outer shells only for interference effects on the first shell.

converged to 2.16(2) Å from 100 to 88% M2 and shortened monotonically with decreasing percentage of M2 to 2.10 Å at 70% M2. The fifth bond distance consistently converged to 2.43(2) Å for all values of M2 site distribution. The outermost, sixth bond distance was widely variable in the fits: It became longer with increasing contribution of the M2 site and ranged between 2.56 and 2.75 Å. Therefore, our estimated error for this peak is large, at ±0.1 Å. Note that 2.75 Å is even longer than the bond distance of the structurally equivalent bond in ferrosilite (Sueno et al. 1976).

On the basis of the results of model A, our best estimate for the Fe distribution between the M2 and M1 [$Fe^{M2}/(Fe^{M2} + Fe^{M1})$] sites is 94%. Though this result differs from that of the preliminary model, $Fe^{M2}/(Fe^{M2} + Fe^{M1}) = 79\%$, we believe it is more accurate because the model-A fits were much more flexible and thorough than the preliminary model, and the $(R\%)^2$ values for model A were consistently lower than those of the preliminary model.

Model B

Model B was designed to determine distortion of the M1 site. Here, the M2 and M1 sites were modeled using four and three Fe-O first-neighbor bond distances, respectively; the rest of the spectrum was modeled by the two theoretical standards, M1outer and M2outer. For this model, we used nine bond distances: one for the first two M2-O bonds, one for the middle two M2-O bond distances, one each for the outer two M2-O bond distances, one bond distance each for the combined first and second, third and fourth, and fifth and sixth atoms in the M1-O site, along with M2outer and M1outer. With the M2 site bond distances fixed in amplitude and position from model A, we ran many fits, in which we cycled through the possibilities of M2 site occupancy, starting at 100% and finishing at 68% M2, in 3% increments. Additionally, for each M2 site occupancy we cycled through values of σ between 0.05 and 0.03 for the peaks representing two bonds. Therefore, the fits had only nine varied parameters: bond lengths for three M1 site peaks, bond lengths for M1outer and M2outer, σ values for M1outer and M2outer, one amplitude, and E_0. Our method of cycling of the fixed variables allowed inspection of the effects of varying two additional parameters (M2 site occupancy and σ). Results of our fits and other data are shown in Table 3. The best fit using this model was for an Fe site distribution of 88% on the M2 site, in fairly good agreement with the results of model A. As can be seen in Table 3, the two shortest bond distances in the M1 site actually shortened relative to the Mg end-member. The errors in the other two distances are large; therefore, these distances are not discussed at length.

TABLE 3. Best fit results for M1 distances: Model B

	Distance (Å)		
Atom*	This study	Mg end-member**	Fe end-member†
O2A	1.96(3)	2.0087	2.090
O1A	(Avg. of O2A and O1A)	2.0279	2.085
O2B	1.98(6)	2.0469	2.124
O1B	(Avg. of O2B and O1B)	2.0657	2.124
O1A	2.24(4)	2.1516	2.195
O1B	(Avg. of O1A and O1B)	2.1709	2.194

* For O-atom positions, refer to Figure 5.
** Pure Mg–end-member (enstatite) bond distances from Ghose et al. (1986).
† Pure Fe–end-member (ferrosilite) from Sueno et al. (1976).

Because model A yielded a best fit with 94% M2 and model B yielded a best fit with 88% M2, we estimate that 92(8)% of the Fe in our sample occupies the M2 site. For comparison, we used other results to estimate the Fe distribution in M2 for orthopyroxene with an Fe/(Fe + Mg) of 0.12. We interpolated between data points from Skogby et al. (1992) and Domeneghetti and Steffen (1992) and obtained distributions of 86% Fe in the M2 site and 14% Fe in the M1 site, well within the range of our fit results.

Error analysis

To evaluate errors in bond distances based on model A, we generated a series of Monte Carlo simulations in which 100–10000 sets of randomly generated starting parameters within a Gaussian probability density were used as input for the fit program (cf. Binder 1984). The parameters of each Gaussian curve were chosen from the range of values we determined in the sequence of fits discussed above. We varied the width of the Gaussian functions (i.e., the error on each parameter) for each parameter to look for changes in the correlation coefficients. Each fit was run with zero iterations. The goal was to compare random numbers from within the probability function to those of our best fit (Table 2) in order to calculate correlation coefficients between each parameter and $(R\%)^2$. If the correlation coefficients for the different parameters are the same, then the relative errors we assigned to the parameters are correct. To a first order, the correlation

coefficients between the individual parameters and $(R\%)^2$ were the same, indicating that errors of ~25% relative for σ, ~1% for the bond lengths, and 8% for the site distribution are accurate approximations.

Figure 7 shows an error surface for a series of fits of the model-A type between 100 and 73% Fe^{M2}/Fe_{tot}. In Figure 7a, the two horizontal axes represent site distribution of Fe and δr, where δr is the shift from the best bond distance obtained from model A (Table 2). For each site distribution of Fe between the M2 and M1 sites, each bond distance was displaced from the ideal bond distance by δr, which ranged between −0.04 and +0.04 Å from the ideal bond distance. The third dimension shows the $(R\%)^2$ value of each fit. In this particular set of fits, the minimum plots at 94% M2, with δr at 0.00. As the figure demonstrates, the $(R\%)^2$ value rapidly increases as δr is increased or decreased, and more gradually increases away from the minimum in Fe site distribution, at 94% M2, consistent with our much narrower constraints on bond distances than on Fe site distribution. Figure 7b shows a cross section of the mesh in Figure 7a at a constant Fe site distribution of 94% M2, and Figure 7c shows a cross section at constant δr of 0.00.

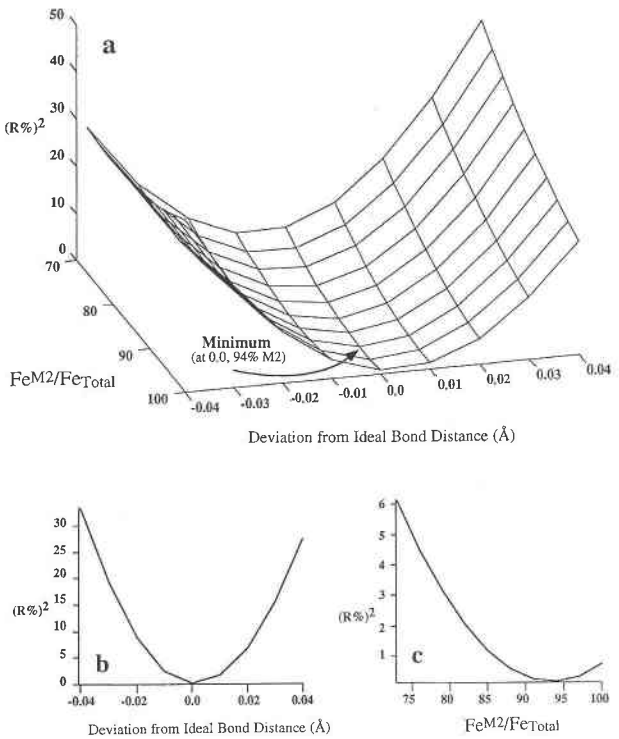

FIGURE 7. (**a**) Error surface of fits using model A. Axes in the horizontal plane include Fe^{M2}/Fe_{tot} and δr, the deviation from the ideal bond length. Bond distances were displaced from ideal values for each Fe^{M2}/Fe_{tot}, in increments of 0.03. Note that the minimum in this series of fits plots at 94% M2 and δr = 0.00. (**b**) $(R\%)^2$ vs. δr at 94% M2. (**c**) $(R\%)^2$ vs. Fe site distribution between 100 and 73% M2, with minimum at 94%, δr constant at 0.0.

DISCUSSION

Individual Fe-O bonds in the M2 site

In the following discussion we refer to the six O-atom types mentioned above: O1a, O1b, O2a, O2b, O3a, and O3b. As shown in Figure 5, the two shortest bonds (1.97 and 1.98 Å) in the M2 site are to O2b and O2a atoms, the intermediate bond lengths (2.09 and 2.16 Å) to O1b and O1a atoms, and the longest bonds (2.43 and 2.65 Å) are to O3a and O3b atoms (Ghose et al. 1986). The O1 atoms are fourfold coordinated, bonded to two M1 cations, one M2 cation, and one Si tetrahedron. These types of O atoms are intermediate in bond strength between O2- and O3-type atoms. O2 atoms are threefold coordinated, bonded to one M1 cation, one M2 cation, and one Si atom. They are underbonded and therefore form stronger bonds than the other O atoms, and their bond lengths are expected to change less in response to changes in pressure, temperature, or composition. O3 atoms are threefold coordinated, forming the bridging O atoms of Si tetrahedral chains, and are also bound to an M2 cation. O3 atoms are overbonded, and thus their bonds are weaker (Hawthorne and Ito 1977; Cameron and Papike 1980; Ghose 1982; Ghose et al. 1986).

On the basis of bond strength, we would expect the shortest bonds to change the least in length and the longest bonds to change the most. Additionally, the type of tetrahedral chain to which each O atom is bound affects its bond-length variability. The A tetrahedral chain has smaller and more distorted tetrahedra and is generally more sensitive to changes in the bonding configuration of the M2 octahedron than the B chain. We show below that when both the bond strength and the tetrahedral chain configuration are considered, the bond lengths determined in this study are consistent with changes expected from the addition of Fe to the Mg–end-member pyroxene.

Our two shortest bond lengths actually shortened relative to both the Fe-O and Mg-O bond lengths for the end-members (Hawthorne and Ito 1977; Sueno et al. 1976; Sasaki et al. 1982; Ghose et al. 1986), but only by 0.02 and 0.04–0.05 Å (Fe-O2b and Fe-O2a, respectively, Table 3). The uncertainty in the Fe-O2b bond length precludes our ability to determine if there is actual shortening relative to the Mg end-member. However, the uncertainty in the Fe-O2a bond length is not large enough to account for the differences in bond length between our sample and either the Mg or Fe end-member. To determine if the contraction resulted from the low temperatures at which we collected the XAFS data (84 K), we extrapolated the volume thermal expansion results of Yang and Ghose (1994) down to 84 K and took the average volume thermal expansion coefficient between 296 and 84 K to be 21×10^{-6}/°C. The bond length shortening we calculated was 0.15%, or 0.003 Å for a bond length of 2 Å. Thus, shortening due to the low temperature of the sample alone cannot account for the differences between our bond lengths and those of the end-members.

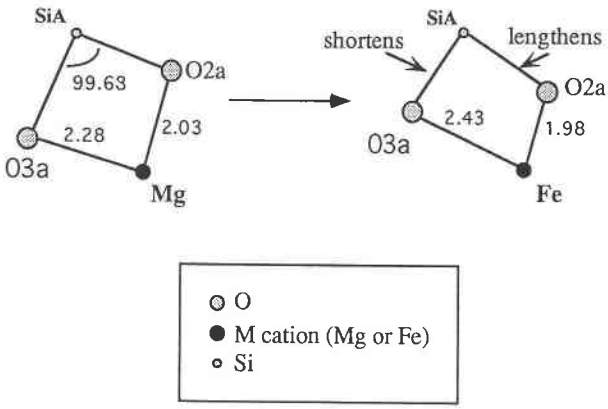

FIGURE 8. Simplified model showing changes in length of M2-O2a and M2-O3a bonds upon substitution of Fe for Mg in the M2 site in orthopyroxene. The M2-O2a bond shortens and the opposing SiA-O2a bond lengthens, whereas the M2-O3a bond lengthens and the opposing SiA-O3a bond shortens. Large shaded circles are O atoms, black circles are M2 cations, small shaded circles are Si atoms.

Bond-length shortening is not unusual for individual bonds in the distorted M2 site. Indeed, the Fe-O2a bond length in ferrosilite is shorter than that of Mg-O2a by 0.01 Å (Table 2). The bond-length shortening relative to the Mg and Fe end-members, especially the shortening of the Fe-O2a bond, can be explained by decreasing distortion of the Si tetrahedra in the A chains and overall expansion of the octahedral layer (Domeneghetti et al. 1985; Sykes-Nord and Molin 1993). The smallest O-Si-O tetrahedral angle in enstatite is 99.68° and is subtended by the O3 and O2 atoms in the A chain, which share an edge with the M2 octahedron (Ghose et al. 1986) as shown in Figure 8. The sharing of the O3a-O2a edge results in contraction of the shared edge relative to other edges in the same tetrahedron and the corresponding edge in B tetrahedra. Therefore, it may be expected that both tetrahedral and octahedral distortions associated with this anomalously small angle and associated Si-Fe repulsion could result in changes of both the Fe-O2a and Fe-O3a bonds, creating a more distorted M2 site and a less distorted A tetrahedron. Indeed, other studies (Smyth 1973; Sykes-Nord and Molin 1993; Bertolo and Nimis 1993) have shown that with the addition of Fe to the orthopyroxene structure the Si-O (nonbridging) bond distances increase, whereas the Si-O (bridging) bond lengths decrease. This is what would be expected if the Fe-O2a (O2a is a nonbridging O atom) bond decreases and the adjacent Fe-O3a (O3a is a bridging O atom) bond increases (Fig. 8). A similar effect was observed by Ohashi et al. (1975) in the monoclinic $CaFeSi_2O_6$-$Fe_2Si_2O_6$ series upon substitution of Ca for Fe.

Additionally, other authors (Domeneghetti et al. 1985; Sykes-Nord and Molin 1993) have postulated that in Fe-rich samples overall changes of the octahedral layer with changes in the M1 site result in straightening of the tetrahedral chains, moving the O3 atoms away from the M2 cation. Thus, a charge imbalance occurs and is compensated by shortening of the other bonds according to the charge-valence model of Pauling. To a lesser extent this could apply to our sample, with shortening of the Fe-O2a and Fe-O2b bonds relative to both the Fe and Mg end-members. Therefore, changes in the Si tetrahedra in the A chains, along with charge-balance adjustments, provide a consistent explanation for the shortening of the Fe-O2 bonds and the lengthening of the Fe-O3 bonds associated with the A tetrahedral chain, and for the less pronounced effect on O atoms bound to the B tetrahedral chain (Cameron and Papike 1981).

The two Fe-O bonds at 2.09 and 2.16 Å correspond to the O1b and O1a atoms (Ghose et al. 1986), respectively, which form a shared edge between the M2 and M1 octahedra. As with the other bond lengths, the bond length associated with the B chain changes less than the bond length associated with the A chain relative to the Mg end-member, with 0.03 and 0.07 Å expansion, respectively.

Individual Fe-O bonds in the M1 site: Indications of the role of Fe^{3+}

The shortest of the M1 bond distances (Table 3), which corresponds to two atoms bound to the A tetrahedral chain, is shortened relative to the Mg end-member. Although this peak represents an average of two bond lengths, it is too small to be accounted for simply by the shortening of only one of the bond lengths. The two shortest M1-O bond lengths in the Mg end-member are 2.01 and 2.03 Å. Therefore, we attribute the shift of this peak toward shorter distances to the contraction of the bonds of both of the atoms represented by this peak relative to the Mg end-member. Though the Fe end-member shows no contraction of either of these two short bonds, the presence of Fe^{3+} in our samples would cause this shortening relative to both the Fe^{2+} and Mg end-members because of cationic radius differences (Shannon and Prewitt 1969). Any Fe^{3+} in the sample is expected to be present in the M1 site (Annersten et al. 1978; Seifert 1983; Tazzoli and Domeneghetti 1987; Saxena et al. 1987). Therefore, we attribute the shortening of the two shortest bonds in our sample to the presence of Fe^{3+}, which results in the M1 portion of the XAFS signal reflecting a sum of M1 sites containing Fe^{3+} and Fe^{2+}. To verify this, we performed bond-valence model calculations for both sites using the method and appropriate parameters described in Brown (1981). Using the bond lengths listed in Table 3, we calculated a valence of 2.78 vu for the M1 site, in accord with the prediction from model B that the M1 XAFS signal represents contributions from both Fe^{2+} and Fe^{3+}. For the M2 site, we calculated a valence of 2.07 vu using the bond lengths in Table 2, suggesting that little or no Fe^{3+} resides in the M2 site.

Bond-length average and distortion

In Table 4 we show the bond-length distortion of our sample, along with that of the two end-members. The

bond-length distortion in our sample, 10.0–15.6 × 10^{-3}, agrees well with the distortion of the Fe end-member and is significantly higher than that of the Mg end-member, 5.71 × 10^{-3}. Additionally, various relationships between octahedral distortions and bond lengths, both individual and average, have been demonstrated in orthopyroxene along the Fe-Mg join (Morimoto and Koto 1969; Brown and Shannon 1973; Hawthorne and Ito 1977; Domeneghetti et al. 1985; Bertolo and Nimis 1993; Sykes-Nord and Molin 1993). To test for linearity of average bond-length expansion along the Fe-Mg join we calculated the average Fe-O bond length (<Fe-O>) for intermediate and end-member orthopyroxene, assuming the <Mg-O> of the end-member (Table 4). Our calculations show that the average Fe-O bond length in the M2 site is constant across the Fe-Mg join, in accord with similar behavior in ionic materials (Boyce and Mikkelsen 1985).

TABLE 4. Tests for linearity of solid solution

Fe/(Mg + Fe)	$Fe^{(M2)}/Fe_{total}$	⟨Fe2-O⟩*	Δ(×10^3)**	Reference†
0.00		2.15 ⟨Mg2-O⟩	5.71	A
0.07	0.970(4)	2.21	—	B
0.12	0.82(6)	2.20–2.23	10.0–15.6	This study‡
0.215(2)	0.820	2.21	—	C
0.39	0.933	2.22	—	B
0.496(3)	0.715	2.22	—	C
1.0		2.23	10.2	D

* ⟨Fe2-O⟩ is the average bond length recalculated in the samples with 0.07, 0.215, and 0.496 Fe/(Fe + Mg) to remove the effect of averaging in Mg-O bond distances. We used the equation ⟨M2-O⟩ = $X Fe^{(M2)}$·⟨Fe2-O⟩ + 1 − $X(Fe^{(M2)})$·⟨Mg2-O⟩ for both samples and assumed ⟨Mg2-O⟩ of the end-member.

** Δ is the distortion parameter and is given by $\Delta = \Sigma [(l_i - l)/l]^2/6$, where i ranges from 1 to 6, l = average bond length, and l_i = individual bond length.

† A = neutron-diffraction data from Ghose et al. (1986); B = Mössbauer and X-ray diffraction data from Skogby et al. (1992); C = Mössbauer data and X-ray diffraction data from Domeneghetti and Steffen (1992); D = X-ray diffraction data from Sueno et al. (1976).

‡ The numbers listed from our study include the two extreme cases in the error on the sixth bond distance, which ranged from 2.55 to 2.73 Å.

Lattice-parameter expansion owing to substitution of Fe for Mg

On comparison of the Fe-O bond lengths in our study with the expansion of the lattice parameters owing to the addition of Fe in the enstatite structure (Sueno et al. 1976; Ghose et al. 1986; Skogby et al. 1992; Domeneghetti and Steffen 1992) it is evident that minor variations and perhaps shrinkage of the shortest Fe-O bonds is consistent with XRD data. The results of XRD studies indicate that the *a* parameter expands the least in terms of percentage expansion and the *b* parameter expands the most. This is consistent with minor contraction of the Fe-O2a and Fe-O2b bonds, which have a component in the *a* direction, combined with expansion of the other four bonds, all of which have components in the *a* direction. The expansion of the *b* parameter can be explained by lengthening of the two Fe-O1 bonds in the M2 octahedron, which shares an edge with an M1 octahedron. This bond lengthening is a likely mechanism for accommodating Fe^{2+}-Mg^{2+} repulsion in adjacent polyhedra and would have a strong component of lengthening in the *b* direction. Lengthening of the Fe-O3a and Fe-O3b bonds would affect both the *b* and *a* parameters, though the smaller expansion of the *a* parameter in comparison with the *b* parameter may indicate that these bonds have a larger component in the *b* direction. Finally, straightening of the tetrahedral chains would have a pronounced effect on the *c* parameter but a small, negative effect on the *b* parameter.

CONCLUSIONS

In comparison with X-ray diffraction, Mössbauer, and neutron-diffraction data, XAFS analysis provides complementary and consistent results for the structure of enstatite. Our analysis provides bond lengths for individual bonds in the M2 site and rough estimates of Fe site distribution. Distortion of the M2 site containing Fe is greater than that of the M2 site in the Mg end-member (Table 4) and may be greater than distortion of the same site in the Fe end-member. Broadly, expansion of the octahedral layers and straightening of the A tetrahedral chain are consistent with the bond lengths we obtained for the M2 site. Fe bonds to O atoms of the tetrahedral A chain were more affected by changes in the M2 site than Fe bonds to O atoms of the B chain, in accord with previous work (Domeneghetti et al. 1985). Additionally, we detected minor contractions of individual Fe-O bond lengths in both the M2 and M1 sites relative to the analogous bond lengths of the Mg end-member, probably a mechanism for charge-balance adjustments and accommodation of smaller cations, respectively. We showed that detailed XAFS analysis involving both XAFS data and XAFS theory provides a useful and unique tool for determination of otherwise uncharacterized structural features in a structure as complicated as that of enstatite. This analysis potentially provides unique structural information for many other mineral structures with local bonding environments that are currently uncharacterized.

ACKNOWLEDGMENTS

This work was supported by NSF and the W.M. Keck Foundation. It is contribution no. 274 of the Institute of Tectonics (Mineral Physics Laboratory) at the University of California, Santa Cruz. We thank the two reviewers for their helpful and thorough comments. We also thank C. Booth, G. Li, and X. Wang for much assistance with data collection and analysis using their FORTRAN programs, and T. Zhang and D. Farber for assistance with the Monte Carlo simulations.

REFERENCES CITED

Annersten, H., Olesch, M., and Seifert, F.A. (1978) Ferric iron in orthopyroxene: A Mössbauer spectroscopic study. Lithos, 11, 301–310.

Bancroft, G.M., and Burns, R.G. (1967) Interpretation of the electronic spectra of iron in pyroxenes. American Mineralogist, 52, 1278–1287.

Bancroft, G.M., Burns, R.G., and Howie, R.A. (1967) Determination of the cation distribution in the orthopyroxene series by the Mössbauer effect. Nature, 213, 1221–1223.

Bertolo, S., and Nimis, P. (1993) Crystal chemical and structural variations in orthopyroxenes from different petrogenetic environments. European Journal of Mineralogy, 5, 707–719.

Binder, K. (1984) Applications of the Monte Carlo method in statistical physics, 311 p. Springer-Verlag, New York.

Boyce, J.B., and Mikkelsen, J.C., Jr. (1985) Local structure of ionic solid solutions: Extended X-ray absorption fine structure study. Physical Review B, 31, 6903–6905.

Bridges, F., Li, G.G., and Wang, X. (1992) Monochromator-induced glitches in EXAFS data: I. Test of the model for linearly tapered samples. Nuclear Instruments and Methods in Physics Research, A320, 548–555.

Bridges, F., Booth, C., and Li, G.G. (1995) An iterative approach to atomic background removal in XAFS data analysis. Physica B, 209, 121–124.

Brown, I.D. (1981) The bond-valence method: An empirical approach to chemical structure and bonding. In M. O'Keeffe and A. Navrotsky, Eds., Structure and bonding in crystals, vol. II, p. 1–30. Academic, New York.

Brown, I.D., and Shannon, R.D. (1973) Empirical bond strength–bond length curves for oxides. Acta Crystallographica, A29, 266–282.

Cameron, M., and Papike, J.J. (1980) Crystal chemistry of silicate pyroxenes. In Mineralogical Society of America Reviews in Mineralogy, 7, 36.

———(1981) Structural and chemical variations in pyroxenes. American Mineralogist, 66, 1–50.

Domeneghetti, M.C., Molin, G.M., and Tazzoli, V. (1985) Crystal-chemical implications of the Mg^{2+}-Fe^{2+} distribution in orthopyroxenes. American Mineralogist, 70, 987–995.

Domeneghetti, M.C., and Steffen, G. (1992) M1, M2 site populations and distortion parameters in synthetic Mg-Fe orthopyroxenes from Mössbauer spectra and X-ray structure refinements. Physics and Chemistry of Minerals, 19, 298–306.

Evans, B.J., Ghose, S., and Hafner, S. (1967) Hyperfine splitting of Fe^{57} and Mg-Fe order-disorder in orthopyroxene ($MgSiO_3$-$FeSiO_3$ solid solution). Journal of Geology, 75, 306–322.

Farges, F. (1995) The site of Fe in Fe-bearing $MgSiO_3$ enstatite and perovskite: A theoretical-, X-ray multiple scattering study at Fe *K*-edge. Physics and Chemistry of Minerals, 22, 318–322.

Farges, F., Guyot, F., Andrault, D., and Wang, Y. (1994) Local structure around Fe in $Mg_{0.9}Fe_{0.1}SiO_3$ perovskite: An X-ray absorption spectroscopy study at the Fe *K*-edge. European Journal of Mineralogy, 6, 303–312.

Ganguly, J., and Ghose, S. (1979) Aluminous orthopyroxene: Order-disorder, thermodynamic properties, and petrologic implications. Contributions to Mineralogy and Petrology, 69, 375–385.

Ghose, S. (1965) Mg^{2+}-Fe^{2+} order in an orthopyroxene, $Mg_{0.93}Fe_{1.07}Si_2O_6$. Zeitschrift für Kristallographie, 122, 81–99.

———(1982) Crystal chemistry. In Advances in Physical Geochemistry, 2, 4–57.

Ghose, S., and Hafner, S. (1967) Mg^{2+}-Fe^{2+} distribution in metamorphic and volcanic orthopyroxenes. Zeitschrift für Kristallographie, 125, 157–162.

Ghose, S., Schomaker, V., and McMullan, R.K. (1986) Enstatite, $Mg_2Si_2O_6$: A neutron diffraction refinement of the crystal structure and a rigid-body analysis of the thermal vibration. Zeitschrift für Kristallographie, 176, 159–175.

Goldman, D.S., and Rossman, G.R. (1976) Identification of a mid-infrared electronic absorption band of Fe^{2+} in the distorted M(2) site of orthopyroxene $(Mg,Fe)SiO_3$. Chemical Physics Letters, 41, 474–475.

———(1977) The spectra of iron in orthopyroxene revisited: The splitting of the ground state. American Mineralogist, 62, 151–157.

Gupta, R.G., and Mendiratta, R.G. (1980) ^{57}Fe Mössbauer study of orthopyroxene of metamorphic origin. Mineralogical Magazine, 43, 815–816.

Hawthorne, F.C., and Ito, J. (1977) Synthesis and crystal-structure refinement of transition-metal orthopyroxenes: I. Orthoenstatite and (Mg, Mn, Co) orthopyroxene. Canadian Mineralogist, 15, 321–338.

Hayes, T.M., and Boyce, J.B. (1982) Extended X-ray absorption fine structure spectroscopy. In Solid State Physics, 37, 173–351.

Kinzler, R.J., and Grove, T.L. (1992a) Primary magmas of mid-ocean ridge basalts: 1. Experiments and methods. Journal of Geophysical Research, 97, 6885–6906.

———(1992b) Primary magmas of mid-ocean ridge basalts: 2. Applications. Journal of Geophysical Research, 97, 6907–6925.

Li, G.G., Bridges, F., and Booth, C.H. (1995) X-ray absorption fine structure standards: A comparison of experiment and theory. Physical Review B, 52, 6332–6348.

Longhi, J. (1991) Comparative liquidus equilibria of hypersthene-normative basalts at low pressure. American Mineralogist, 76, 785–800.

Molin, G.M. (1989) Crystal-chemical study of cation disordering in Al-rich and Al-poor orthopyroxenes from spinel lherzolite xenoliths. American Mineralogist, 74, 593–598.

Morimoto, N., and Koto, K. (1969) The crystal structure of orthoenstatite. Zeitschrift für Kristallographie, 129, 65–83.

Mottana, A., Paris, E., and Anovitz, L.M. (1990) Fe^{2+}-Mg^{2+} order-disorder in natural and heated orthopyroxenes: Determination by synchrotron X-ray absorption spectroscopy. Eos, 71, 1621.

Mustre de Leon, J., Rehr, J.J., and Zabinsky, S.I. (1991) Ab initio curved-wave X-ray absorption fine structure. Physical Review B, 9, 4146–4156.

Ohashi, Y., Burnham, C.W., and Finger, L.W. (1975) The effect of Ca-Fe substitution on the clinopyroxene crystal structure. American Mineralogist, 60, 423–434.

Pollack, S.S., and Rubie, W.D. (1964) X-ray identification of ordered and disordered ortho-enstatite. American Mineralogist, 49, 983–992.

Rehr, J.J., and Albers, R.C. (1990) Scattering-matrix formulation of curved-wave multiple-scattering theory: Application to X-ray absorption fine structure. Physical Review B, 41, 8139–8149.

Rehr, J.J., Mustre de Leon, J., Zabinsky, S.I., and Albers, R.C. (1991) Theoretical X-ray absorption fine structure standards. Journal of the American Chemical Society, 113, 5135–5140.

Rossman, G.R. (1980) Pyroxene spectroscopy. In Mineralogical Society of American Reviews in Mineralogy, 7, 93–113.

Sasaki, S., Takeuchi, Y., Fujino, K., and Akimoto, S. (1982) Electron-density distributions of three orthopyroxenes, $Mg_2Si_2O_6$, $Co_2Si_2O_6$, and $Fe_2Si_2O_6$. Zeitschrift für Kristallographie, 158, 279–297.

Saxena, S.K., Tazzoli, V., and Domeneghetti, M.C. (1987) Kinetics of Fe^{2+}-Mg distribution in aluminous orthopyroxenes. Physics and Chemistry of Minerals, 15, 140–147.

Seifert, F. (1983) Mössbauer line broadening in aluminous orthopyroxenes: Evidence for next nearest neighbors interactions and short-range order. Neues Jahrbuch für Mineralogie Abhandlungen, 148, 141–162.

Shannon, R.D., and Prewitt, C.T. (1969) Effective ionic radii in oxides and fluorides. Acta Crystallographica, B25, 925–936.

Skogby, H., Annersten, H., Domeneghetti, M.C., Molin, G.M., and Tazzoli, V. (1992) Iron distribution in orthopyroxene: A comparison of Mössbauer spectroscopy and X-ray refinement results. European Journal of Mineralogy, 4, 441–452.

Smyth, J.R. (1973) An orthopyroxene structure up to 850 °C. American Mineralogist, 58, 636–648.

Stern, E.A. (1993) Number of relevant independent points in X-ray absorption finestructure spectra. Physical Review B, 48, 9825–9827.

Stolper, E. (1980) A phase diagram for mid-ocean ridge basalts: Preliminary results and implications for petrogenesis. Contributions to Mineralogy and Petrology, 74, 13–27.

Sueno, S., Cameron, M., and Prewitt, C.T. (1976) Orthoferrosilite: High-temperature crystal chemistry. American Mineralogist, 61, 38–53.

Sykes-Nord, J.A., and Molin, G.M. (1993) Mg-Fe order-disorder reaction in Fe-rich orthopyroxene: Structural variations and kinetics. American Mineralogist, 78, 921–931.

Tazzoli, V., and Domeneghetti, M.C. (1987) Crystal-chemistry of natural and heated aluminous orthopyroxenes. Physics and Chemistry of Minerals, 15, 131–139.

Teo, B.K. (1986) EXAFS: Basic principles and data analysis. In Inorganic Chemistry Concepts, 9, 349 p. Springer-Verlag, New York.

Ukhanov, A.V., and Malysheva, T.V. (1973) Mössbauer ^{57}Fe data for orthopyroxenes and the heating of ultrabasite xenoliths in a kimberlite magma. Geochemistry International, 10, 1105–1109.

Virgo, D., and Hafner, S.S. (1968) Re-evaluation of the cation distribution in orthopyroxenes by the Mössbauer effect. Earth and Planetary Science Letters, 4, 265–269.

Virgo, D., and Hafner, S.S. (1970) Fe^{2+},Mg order-disorder in natural orthopyroxenes. American Mineralogist, 55, 201–223.

von Seckendorff, V., and O'Neill, H.St.C. (1993) An experimental study

of Fe-Mg partitioning between olivine and orthopyroxene at 1173, 1273, and 1423 K and 1.6 GPa. Contributions to Mineralogy and Petrology, 113, 196–207.

Waychunas, G.A., Apted, M.J., and Brown, G.E. (1983) X-ray *K*-edge absorption spectra of Fe minerals and model compounds: Near-edge structure. Physics and Chemistry of Minerals, 10, 1–9.

Waychunas, G.A., Brown, G.E., and Apted, M.J. (1986) X-ray *K*-edge absorption spectra of Fe minerals and model compounds: II. EXAFS. Physics and Chemistry of Minerals, 13, 31–47.

Yang, H., and Ghose, S. (1994) Thermal expansion, Debye temperature and Gruneisen parameter of synthetic $(Fe,Mg)SiO_3$ orthopyroxenes. Physics and Chemistry of Minerals, 20, 575–586.

Manuscript received April 28, 1995
Manuscript accepted August 2, 1996